# An Information Flow Switching-Based Despeckling Network Under Real Dual-Polarization SAR Conditions

Liupeng Lin, Huanfeng Shen, *Senior Member, IEEE*, Jie Li, *Member, IEEE*, Jingan Wu, Shaowei Shi, and Qiangqiang Yuan, *Member, IEEE*

***Abstract*— Polarimetric synthetic aperture radar (SAR) can capture rich polarization information of targets, but it is inherently affected by speckle. Learning-based methods have demonstrated superior speckle suppression potential. Most existing methods use optical images to simulate SAR noise for model training. Because of the significant differences in the imaging mechanisms between optical and SAR images, the data characteristics of these two types differ significantly, resulting in poor generalization performance. To this end, an Information Flow Switching-based Despeckling Network (IFSDN) is proposed for dual-polarization SAR image. By using the long time series data, the first dual-polarization SAR real dataset is constructed. The hybrid feature extraction module (HFEM) is constructed to independently extract and integrate features from both the diagonal and nondiagonal elements of the covariance matrix. Additionally, the multihierarchical residual attention despeckling (MRAD) module performs despeckling on feature maps from low to high levels. On this basis, the information flow switching mechanism facilitates the interaction of dominant features before and after despeckling, injecting spatial details into the despeckled results, reducing speckle noise, and preserving polarization information. By considering temporal changes, an adaptive joint loss function is, furthermore, constructed to guide the network training process, achieving high-fidelity despeckling while maintaining spatial-polarization information. Experiments show that IFSDN outperforms existing state-of-the-art methods in the speckle removal task for real dual-polarization SAR images, which can effectively preserve spatial and polarization information while suppressing speckles. Besides, generalization experiments demonstrate that the proposed model can be effectively applied to diverse datasets across various climate zones, showcasing its strong robustness.**

***Index Terms*— Deep learning, dual-polarization SAR (Dual-SAR) image despeckling, information flow switching mechanism, real synthetic aperture radar (SAR) data, remote sensing.**

Received 3 September 2024; revised 25 November 2024 and 5 January 2025; accepted 2 February 2025. Date of publication 7 February 2025; date of current version 27 February 2025. This work was supported in part by the National Natural Science Foundation of China under Grant 42301417, Grant 42130108, and Grant 42471504; in part by Hubei Provincial Key Research and Development Program under Grant 2023BAB066; and in part by Guangdong Basic and Applied Basic Research Foundation under Grant 2022A1515110095. *(Corresponding authors: Huanfeng Shen; Jie Li.)*

Liupeng Lin and Huanfeng Shen are with the School of Resource and Environmental Sciences, Wuhan University, Wuhan 430079, China (e-mail: linliupeng@whu.edu.cn; shenhf@whu.edu.cn).

Jie Li, Shaowei Shi, and Qiangqiang Yuan are with the School of Geodesy and Geomatics, Wuhan University, Wuhan 430079, China (e-mail: jli89@sgg.whu.edu.cn; 2017301610139@whu.edu.cn; qqyuan@sgg.whu.edu.cn).

Jingan Wu is with the School of Geospatial Engineering and Science, Sun Yat-sen University, Zhuhai 519082, China (e-mail: wujg5@mail.sysu.edu.cn).

Digital Object Identifier 10.1109/TGRS.2025.3539840

## I. Introduction

SYNTHETIC aperture radar (SAR) is a widely used active microwave remote sensing observation platform that can continuously observe the Earth's surface through microwave coherent imaging all day and all day [1], [2]. Polarization SAR, in particular, provides richer backscattering information about ground objects through different signal transmission and reception modes, facilitating better target interpretation and inversion analysis of surface physical parameters. Consequently, SAR images play a crucial role in target detection [3], [4], disaster assessment [5], [6], land use and land cover classification [7], [8], ecological environment monitoring [9], [10], [11], and more. Because of the characteristics of signal coherent imaging, there is inherent speckle noise in SAR images, which, however, seriously pollutes SAR images and limits their potential in applications [12]. It is, therefore, essential to suppress speckles in SAR images.

Current despeckling methods can be classified into filter-based, variation-based, and learning-based methods. Early filter-based SAR image despeckling techniques primarily relied on local spatial filtering. One classic example is the linear minimum mean squared error (LMMSE) filtering algorithm, which uses the local statistical properties of multiplicative noise. This algorithm led to the development of several classic algorithms, such as the Lee filter [1], Frost filter [13], Kuan filter [14], and Sigma filter [15]. These algorithms employ the statistical characteristics of noise to minimize the mean squared error between the real value and the estimated value, determining the coefficients in the linear relationship between the filtering result and the original image to achieve despeckling. Building on this foundation, some researchers have extended these methods to fully polarimetric SAR images, resulting in techniques like IDAN [16], polarized refined Lee filtering [17], and polarized refined Sigma filtering [18]. While SAR image despeckling methods based on the LMMSE estimator are known for their simplicity and efficiency, they struggle to balance speckle suppression and edge preservation due to their simplistic noise model assumptions.

Subsequently, to leverage the polarization and structural similarity between pixels, researchers focused on nonlocal mean SAR image filtering. These methods estimate the target pixel by searching for similar pixels within a nonlocal window and performing a weighted average of the found similar pixels. For single-polarization SAR image

speckle suppression, Deledalle et al. [19] proposed the probabilistic patch-based (PPB) method, which determines the weight of similar pixels by considering the differences between similar pixels and the target pixel during iterative solution, thus achieving SAR image despeckling. Because of its excellent performance in single-polarization SAR, the PPB method has been extended to PolSAR images. The SAR Block Matching and 3-D filtering (SAR-BM3D) [20] combines the nonlocal algorithm with LMMSE denoising in the wavelet domain. In multipolarization SAR despeckling, the PolSAR nonlocal means filtering method uses the characteristic that PolSAR data follow a complex Wishart distribution. It measures pixel similarity through a similarity ratio hypothesis test, sets a threshold based on this similarity, and excludes pixels outside the threshold from the filtering process. Zhong et al. [21] combined the advantages of nonlocal means and distributed Lee filtering to fully account for the overall and internal structural differences between similar blocks. Generally, nonlocal mean filtering algorithms offer better filtering effects, but they have high computational complexity, are prone to oversmoothing and block effects, and can cause point targets to become defocused and blurred.

The variation-based methods establish the energy function between the observed value and the real value, which includes data fidelity terms and prior terms, and achieve the goal of denoising by optimizing the energy function [22], [23]. In single-polarization SAR image denoising, Aubert and Aujol [24] were the first to introduce a variational model into SAR intensity image despeckling, namely, the AA model. Subsequently, Shi and Osher [25] proposed the SO model, using total variation priors to solve the model in the logarithmic domain. Ma et al. [26] proposed the Adaptive Nonlocal Functionals (ANLFs) model, incorporating nonlocal self-similarity priors for model resolution. Nie et al. [27] proposed the first variational model for the PolSAR polarization covariance matrix, namely the WisTV-C model. This model leverages the statistical properties of the Wishart probability distribution function and the maximum posterior probability framework to derive a PolSAR total variation regularization term. The variational model is then solved using variable splitting and alternating minimization techniques. Variation-based despeckling methods effectively balance speckle removal and spatial detail preservation; however, they tend to produce artifacts in heterogeneous areas and have relatively low processing efficiency.

With the development of computing power, deep learning has made gratifying progress in the field of SAR image processing with its powerful capabilities in fitting nonlinear relationships and feature representation [28], [29], [30], [31]. The learning-based despeckling methods learn the mapping function between noisy images and clean images through a large amount of driving data and then apply the converged model to the noisy images to achieve speckle removal. Generally, the learning-based methods adopt the following three strategies for network model learning. The first strategy involves directly learning the multiplicative noise model between noisy and clean SAR images through the network. Wang et al. [32] proposed the division residual network, which replaces the addition operation of the original residual network with the division operation. deSpeckNet [33] directly generates clean images and noisy images through two branch networks, applying a multiplicative noise model to constrain the loss function. The second strategy rewrites the multiplicative noise model as an additive noise model. This approach converts multiplicative noise, which has a mean value of 1 and a stationary variance, into additive noise with a mean value of 0 and nonstationary variance. The network model is then used to remove the noise. Zhang et al. [34] proposed a residual neural network with seven dilated convolutions to remove speckles from SAR images, using dilated convolutions to increase the receptive field size. Hybrid Dilated Residual Attention Network (HDRANet) [35] couples dilated convolution and attention mechanisms to enhance the network's global information perception and calibrate feature maps. The third strategy involves networks based on homomorphic transformation, which perform a logarithmic transformation on SAR images to convert multiplicative noise into additive noise, enabling subsequent speckle removal. Chierchia et al. [36] used a network with 17 convolutional layers to denoising the logarithmically transformed noisy image, followed by an exponential transformation to obtain the filtered image. On this basis, Dalsasso et al. [37] further considered the Fisher–Tippett distribution characteristics of SAR images. This strategy has been extended to polarimetric SAR images. The MUltichannel LOgarithm with Gaussian denoising (MuLoG) [38] framework performs matrix logarithmic transformation on polarimetric SAR images, then uses Wishart–Fisher–Tippett denoiser for denoising, and obtains filtered covariance matrices through matrix exponential transformation. Under this framework, Tucker and Potter [39] used a CNN network to replace the Wishart–Fisher–Tippett denoiser to achieve speckle removal from fully polarimetric SAR images.

In the existing supervised learning paradigm, most methods adopt optical image simulation noise to construct "multiplicative noisy image-clean image" training sample pairs. Because of the different imaging mechanisms between optical images and SAR images, there are significant differences in data characteristics and distribution between the two. Consequently, models trained on these simulated datasets often fail to meet the despeckling needs of real SAR images. Most deep learning despeckling methods are, furthermore, based on simulated single-polarization SAR intensity image datasets, leaving dual-polarization SAR or full-polarimetric SAR image datasets largely unexplored. Currently, deep learning methods often transplant optical image denoising networks to SAR images, without developing specialized network structures tailored to the numerical characteristics of SAR images. Besides, existing methods do not fully consider the correlation and redundancy of features extracted from each polarization channel. To this end, this article adopts long-time series dual-polarization SAR images to establish a dual-polarization SAR "noisy image-temporal average label image" sample dataset. Based on this dataset, an information flow switching-based despeckling network (IFSDN) is constructed to perform dual-polarization covariance matrix despeckling. The contributions of the proposed despeckling framework mainly include the following three aspects.

1) Combined with the long-term series data, a real dual-polarization SAR data sample dataset is established.

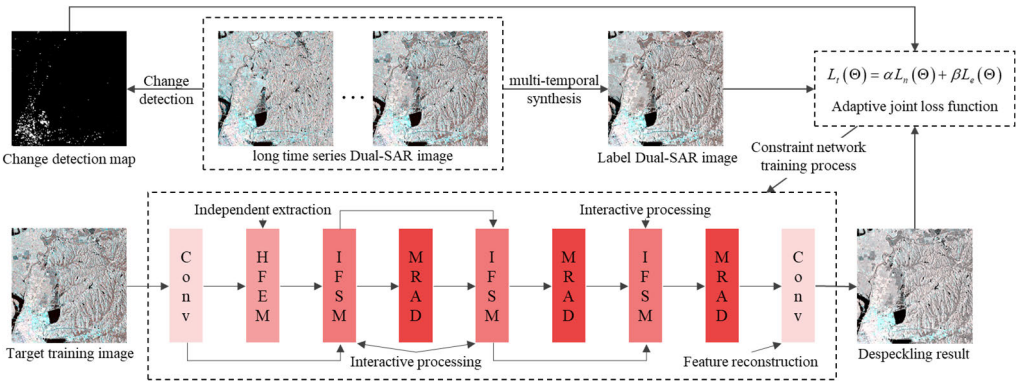


Fig. 1. Overall architecture diagram of IFSDN.

Oriented to the real SAR data conditions, a despeckling convolution network based on the information flow switching is constructed.

2) Under the end-to-end despeckling framework, a dual-SAR hybrid feature extraction module (HFEM) is designed to independently process the diagonal elements and nondiagonal elements of the dual-polarization SAR covariance matrix. Subsequently, the independently processed feature maps are integrated and reconstructed. Besides, the multihierarchical residual attention module is constructed to perform multilevel feature map despeckling.
3) In terms of spatial information reconstruction, the information flow switching mechanism is coupled with the multihierarchical residual attention despeckling (MRAD) module to interactively weight the feature maps before and after despeckling. This process injects spatial detail into the despeckled results and enhances polarization information. Besides, an adaptive joint loss function based on change detection is proposed, which fully considers the numerical changes in label data caused by temporal variations.

The rest of this article is organized as follows. Section II describes the degradation model and data organization. Section III delves into the details of the despeckling framework for real dual SAR. Section IV presents experiments conducted across four seasons and four cities, comparing results with five mainstream algorithms, followed by the discussion in Section V. The conclusion and future work are provided in Section VI.

## II. Degradation Model

According to the fully polarimetric SAR image theory, under the condition of satisfying reciprocity, the complex scattering vector $u$ can be expressed as [1]

$$u = \left[S_{\mathrm{hh}}, \sqrt{2}S_{\mathrm{hv}}, S_{\mathrm{vv}}\right]^T \tag{1}$$

where $S_{\mathrm{hh}}$ and $S_{\mathrm{vv}}$ represent power return in the copolarized channels, $S_{\mathrm{vh}}$ is power return in the cross-polarized channels. A reciprocal medium $u$ follows a zero-mean multivariate complex, and the Gaussian probability density function is as follows [1]:

$$p(u) = \frac{1}{\pi^3|C|}\exp\left(-u^{\dagger}C^{-1}u\right) \tag{2}$$

where $C$ denotes complex covariance matrix, and $^{\dagger}$ represents the complex conjugate transpose. For the polarimetric SAR covariance matrix $C$, the diagonal terms of the matrix follow a multiplicative noise model, and the off-diagonal terms can be modeled by a combination of additive and multiplicative noise models [40]. In this article, the mapping relationship between the observed polarization SAR covariance matrix $C_y$ and the noise-free polarization SAR covariance matrix $C_x$ is constructed, and the polarimetric SAR image noise model is modeled as: $C_y = f_s(C_x)$. For dual-polarization data, such as Sentinel-1 data, the complex scattering vector $u$ reduces to $u = [S_{\mathrm{vv}}, \sqrt{2}S_{\mathrm{hv}}]^T$, the covariance matrix $C_{\mathrm{dual}}$ of the dual-polarization SAR data can be defined as follows [41]:

$$C_{\mathrm{dual}} = \begin{bmatrix} \langle S_{\mathrm{vv}}S_{\mathrm{vv}}^* \rangle & \langle S_{\mathrm{vv}}S_{\mathrm{vh}}^* \rangle \\ \langle S_{\mathrm{vh}}S_{\mathrm{vv}}^* \rangle & \langle S_{\mathrm{vh}}S_{\mathrm{vh}}^* \rangle \end{bmatrix} \tag{3}$$

where $C_{\mathrm{dual}}$ represents the dual-polarization SAR covariance matrix. $\langle . \rangle$ represents spatial statistical averaging operator, and $*$ represents the conjugate operation. In the proposed method, the real and imaginary parts of the upper triangular matrix of the covariance matrix are extracted to obtain the SAR covariance value matrix as below so that each element of the covariance matrix can be processed equally and independently

$$C_{\mathrm{val}} = \begin{bmatrix} C_{11} & C_{12r} & C_{12i} & C_{22} \end{bmatrix}^T \tag{4}$$

where the subscript indicates its position in the covariance matrix $C_{\mathrm{dual}}$, $C_{12r}$ is the real part value, and $C_{12i}$ is the imaginary part value. $[.]^T$ is the transpose operation.

## III. Dual-Polarization SAR Despeckling Framework Under Real Data Conditions

This article proposes a dual-polarization SAR despeckling framework designed to bridge the gap between training models under simulated data conditions and applying models in real scenarios. As illustrated in the upper part of Fig. 1, within this framework, long time series data are used to construct real dual-polarization SAR training and test datasets, employing the strategy of "noisy images-multitemporal average images" for network training. As illustrated in the lower part of Fig. 1, in the despeckling network, the HFEM is constructed to independently extract features from each element of the covariance matrix and integrate all-element features. The MRAD module is designed to perform feature maps denoising from low levels

to high levels. On this basis, the information flow switching module (IFSM) facilitates the exchange of dominant features in the feature maps before and after denoising, promoting the interaction of beneficial information flow. An adaptive joint loss function based on temporal changes is proposed to constrain network training, ensuring high fidelity speckle removal from dual-polarization SAR images while preserving spatial-polarization information. The details of the despeckling framework are as follows.

### A. Real Dataset Construction

Because of the limitation of the SAR imaging mechanism, there is inherent speckle noise in SAR images. Existing optical simulation SAR data cannot correctly represent the backscattering coefficient of the ground objects, resulting in poor model generalization when applied to real scenes. Based on long time series SAR images, this article, therefore, obtains clean SAR images through multitemporal synthesis, and then generates a real dual-polarization SAR "noisy image-clean image" sample dataset. For data availability reasons, the Sentinel-1, which provides C-band dual-polarization SAR data, is adopted as the primary data source. Among the two types of Sentinel-1 Level-1 products, single look complex (SLC) data is chosen over the ground range detected (GRD) data due to its richer spatial detail information and retention of phase information; thence, the level-1 SLC data obtained with terrain observation with progressive scan technology (TOPS) in interferometric wide swath (IW) mode is used for real dataset construction. The dataset construction process is as follows.

1) *Precise Orbit Correction.* Since the orbit state vector in the metadata of the raw SAR product is usually inaccurate, this processing can be used to refine the orbit state vector.
2) *Radiation Calibration:* This process corrects the radiometric bias of the level 1 image to generate pixel values of the SAR image that can truly represent the radar backscatter of the reflecting surface. In this article, the complex radiometric calibration is adopted for radiometric correction of dual-polarization SAR images.
3) *TOPS-Deburst:* The SLC products obtained by TOPS technology have multiple swaths, with each subswath image is composed of bursts. TOPS-Deburst operation concatenates the bursts and merges the effective parts of adjacent subswaths to generate a full-scene SAR image.
4) *Polarimetric Matrices Generation:* Dual-polarization SAR covariance matrices $C_{\text{dual}}$ [41] are generated.
5) *Multilook Processing:* This process performs multilook processing on range and azimuth directions, and generate ground range square pixels. It is worth mentioning that the main goal of multilook processing in this article is to generate ground range square pixels, not to suppress speckle noise.
6) *Terrain Correction:* Terrain correction is performed by using SRTM worldwide elevation data, and the pixel spacing of the data is resampled to 15 m. The SRTM Plus V3 products with 1-arc-second resolution are adopted for terrain correction.
7) *Data Registration:* Multitemporal data in the same area are spatially registered.

TABLE I
SATELLITE IMAGE PARAMETER INFORMATION

| Mission | Sentinel-1A |
|---|---|
| Acquisition Mode | IW |
| Band | C |
| Product Type | SLC |
| Looks | 1 |
| Antenna Pointing | Right |
| Spacing (resample) | 15×15m |
| Polarimetric Mode | VH/VV |
| Radar Centre Frequency | 5.405GHz |

TABLE II
IMAGE ACQUISITION TIME INFORMATION

| Sentinel-1A (MM/DD/YY) | | | | |
|---|---|---|---|---|
| 05/02/2020 | 05/14/2020 | 05/26/2020 | 06/07/2020 | 06/19/2020 |
| 07/01/2020 | 07/13/2020 | 07/25/2020 | 08/06/2020 | 08/18/2020 |
| 08/30/2020 | 09/11/2020 | 09/23/2020 | 10/05/2020 | 10/17/2020 |
| 10/29/2020 | 11/10/2020 | 11/22/2020 | 12/04/2020 | 12/16/2020 |
| 12/28/2020 | 01/09/2021 | 01/21/2021 | 02/02/2021 | 02/14/2021 |
| 02/26/2021 | 03/10/2021 | 03/22/2021 | 04/03/2021 | 04/15/2021 |
| 04/27/2021 | 05/09/2021 | 05/21/2021 | 06/02/2021 | 06/14/2021 |

8) *Change Detection Mask Extraction:* This process is used to distinguish changing areas and nonchanging areas in multitemporal data and generate the change detection masks.
9) *"Noisy Data-Label Data-Change Detection Mask" Pairing and Dataset Generation:* This processing mainly involves pairing the above processed data and performing necessary trimming on the paired data to facilitate network model training.

Based on the aforementioned processing steps, Wuhan, China, and its adjacent areas are selected as the research area. This area contains a variety of surface cover types, such as urban built-up areas, cropland, forests, shrubs, grassland, water bodies, and bare land, which can meet the surface cover diversity requirements of the training dataset. At the same time, the selected area of the dataset covers common scattering mechanisms, including homogeneous areas and heterogeneous areas. The long-time series dual-polarization SAR images of the Wuhan area acquired by Sentinel-1 serve as experimental data. The detailed parameters of the satellite images used in the experiment are shown in Table I. The 35 data with a period of one year are used to construct the sample dataset. The data acquisition time is shown in Table II. Three regions with different land surface types in various climate zones are, furthermore, chosen to generate generalization experimental data, including Xi'an, China, located in the temperate monsoon zone; Guangzhou, China, located in the subtropical monsoon zone; and Hainan Island, China, located in the tropical monsoon zone. The preprocessing steps for constructing the real dataset are carried out using SNAP software version 10.0.0, provided by the European Space Agency (ESA). All parameter settings in these preprocessing steps are set to the default values officially provided by SNAP.

### B. Dual-Polarization SAR HFEM

López-Martínez and Fabregas [40] have mathematically demonstrated that there are significant differences in the

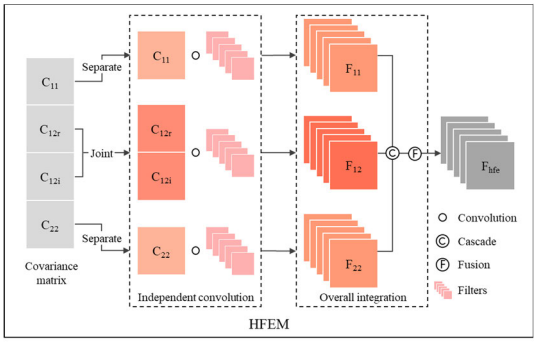


Fig. 2. HFEM module.

noise models of diagonal elements and nondiagonal elements in the dual-polarization SAR covariance matrix. The diagonal elements of the covariance matrix are subject to the multiplicative noise model, while the off-diagonal elements follow a combined model of multiplicative noise and additive noise; therefore, the dual-polarization SAR HFEM is designed. Under this module, the independent complex relationship mapping layer is constructed to extract features from both diagonal elements and nondiagonal elements, addressing the distribution differences of various noise models, and thereby obtaining more accurate feature mapping. In the HFEM, as shown in Fig. 2, under satisfying the reciprocity condition, three independent complex relationship mapping layers are constructed to extract features of two diagonal elements and one nondiagonal element, respectively, including real value features of diagonal intensity information and the complex characteristics of off-diagonal phase difference information, which can be modeled as

$$F_{11} = C_{11} \circ w^1_{\text{hfe}} + b^1_{\text{hfe}} \tag{5}$$

$$F_{12} = f_{\text{cat}}(C_{12r}, C_{12i}) \circ w^2_{\text{hfe}} + b^2_{\text{hfe}} \tag{6}$$

$$F_{22} = C_{22} \circ w^3_{\text{hfe}} + b^3_{\text{hfe}} \tag{7}$$

where $F_{11}$ and $F_{22}$ represent the feature maps of two diagonal elements respectively, and $F_{12}$ is the feature maps of nondiagonal elements, and $\circ$ denotes the convolutional operator. The proposed method separates and extracts the real and imaginary parts of the nondiagonal elements to obtain real-valued images so as to avoid the potential accuracy loss that can occur when real-valued networks process complex-valued images.

Subsequently, the three feature maps are cascaded. Full element feature integration and information compression are performed to optimize features and reduce the number of network parameters. The specific process is as follows:

$$F_{\text{hfe}} = f_{\text{cat}}(F_{11}, F_{12}, F_{22}) \circ w^4_{\text{hfe}} + b^4_{\text{hfe}} \tag{8}$$

where $f_{\text{cat}}(.)$ denotes the element cascade operator, $w^1_{\text{hfe}}$, $w^2_{\text{hfe}}$, $w^3_{\text{hfe}}$, $w^4_{\text{hfe}}$ and $b^1_{\text{hfe}}$, $b^2_{\text{hfe}}$, $b^3_{\text{hfe}}$, $b^4_{\text{hfe}}$, respectively, represent the weights and bias terms of each convolutional layer of the HFEM.

### C. MRAD Module

An MRAD module is proposed to effectively suppress speckles in dual-polarization SAR feature maps. This module uses three layers of residual convolution blocks (RCBs)

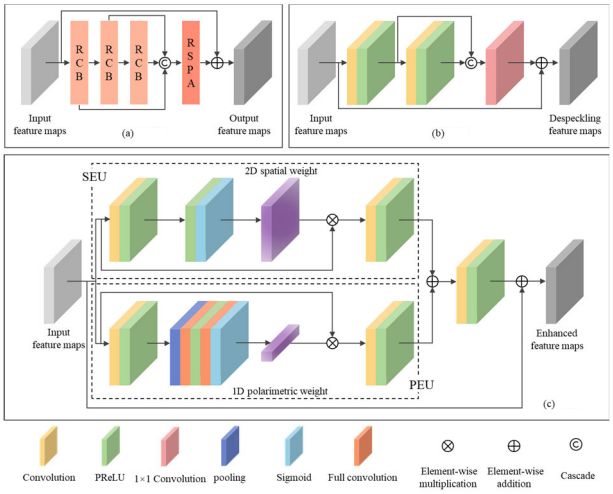


Fig. 3. MRAD module. Among them, (a) architecture diagram of MRAD, (b) RCB module, and (c) RSPA module.

to filter low-, medium-, and high-level features, effectively reducing speckles. The filtered feature maps are then fused through cascade processing for multilevel speckle removal. In order to enhance key features and reduce redundant features, a residual spatial and polarization attention mechanism (RSPA) recalibrates feature weights in both spatial and polarization dimensions.

As shown in Fig. 3(b), the RCB module consists of three convolutional layers. The first two convolutional layers are used for progressive feature map filtering. Since spatial detail information may be lost during the despeckling, the outputs of two convolution filtering are cascaded to jointly process despeckled features at different levels, enhancing the reusability of spatial details. Subsequently, the $1 \times 1$ convolution is used to perform dimensionality reduction on the cascaded features. Finally, the residual structure is employed for local feature concatenation to introduce original features back into the network. In the RSPA module, a spatial enhancement unit (SEU) recalibrates the spatial weight, producing spatially enhanced feature maps, which can be modeled as

$$F_{\text{seu}} = f_{\text{mul}}\left(F_{\text{in}}, \xi\left(F_{\text{in}} \circ w^1_{\text{seu}} + b^1_{\text{seu}}\right)\right) \tag{9}$$

where $F_{\text{seu}}$ represents the spatial-enhanced feature maps, $F_{\text{in}}$ is the input feature map, $f_{\text{mul}}(.)$ represents the element multiplication operator, $\xi(.)$ denotes the Sigmoid normalization function. $w_{\text{seu}}$ and $b_{\text{seu}}$ are the convolution kernel weight and bias term of the SEU, respectively.

In order to process polarization information equally, the polarization enhancement unit (PEU) is built in parallel to recalibrate the polarization weight of feature maps to obtain polarization-enhanced feature maps, which can be formulated as

$$F_{\text{peu}} = f_{\text{mul}}\left(F_{\text{in}}, \xi\left(\left(f_{\text{mp}}(F_{\text{in}}) \circ w^1_{\text{peu}} + b^1_{\text{peu}}\right) \circ w^2_{\text{peu}} + b^2_{\text{peu}}\right)\right) \tag{10}$$

where $F_{\text{peu}}$ represents the polarization-enhanced feature maps, $f_{\text{mp}}(.)$ represents the maximum pooling operator, $w^1_{\text{peu}}$ and $w^2_{\text{peu}}$ represent the weight of the sparse fully connected layer and the dense fully connected layer, respectively, $b^1_{\text{peu}}$ and $b^2_{\text{peu}}$ represent the corresponding bias items.

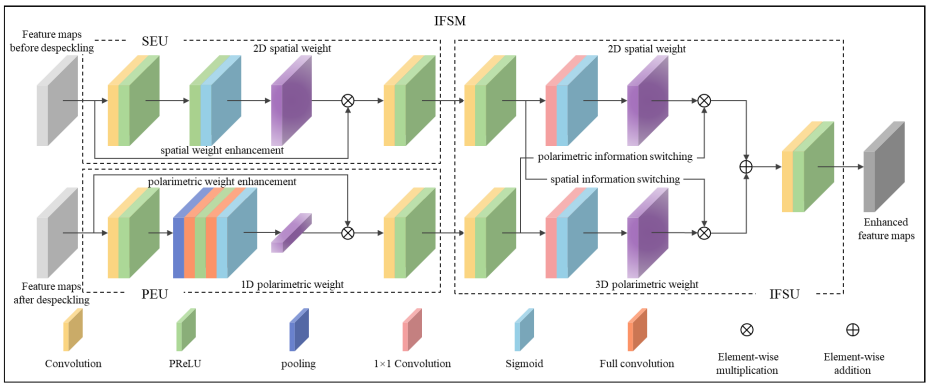


Fig. 4. IFSM module.

By performing feature fusion on the above two parallel enhanced feature maps and using the residual structure to achieve original feature reuse, the RSPA module can be expressed mathematically as

$$F_{\text{rspa}} = f_{\text{add}}\left(F_{\text{in}}, f_{\text{add}}\left(F_{\text{seu}}, F_{\text{peu}}\right) \circ w_{\text{rspa}} + b_{\text{rspa}}\right) \tag{11}$$

where $f_{\text{add}}(.)$ is the element-wise addition operator, $w_{\text{rspa}}$ and $b_{\text{rspa}}$, respectively, represent the convolution kernel weight and bias term of the RSPA module.

### D. Information Flow Switching Mechanism

The attention mechanism is a widely used feature weight recalibration mechanism [42], [43] that can effectively increase the weight of key features. Among various attention mechanisms, cross-attention [44], [45], as a weighting mechanism for the dominant features of multisource data, has been successfully applied in image fusion tasks. In the dual-polarization SAR image despeckling task, the feature map processed by the despeckling module inevitably loses spatial detail information, whereas the feature map before despeckling retains rich spatial detail despite significant noise; thus, effectively reconstructing spatial detail information while removing speckle presents a major challenge. In order to address this, inspired by the cross-attention mechanism, this article proposes an information flow switching mechanism. This mechanism aims to make full use of the texture information of the feature map before despeckling through information interaction, guiding the reconstruction of spatial information in the feature map after despeckling. In the multilayer residual attention module, after despeckling the feature maps at different levels, the IFSM is embedded in turn to guide their spatial information reconstruction. Simultaneously, the despeckled polarization information is injected into the feature maps before despeckling, maintaining its polarization characteristics while reducing the impact of speckle noise. Additionally, the IFSM is also embedded after the dual-polarization SAR HFEM to improve the use of polarization information in the hybrid feature maps.

The IFSM comprises three basic units: the SEU, the PEU and the information flow switching unit (IFSU), as shown in Fig. 4. The SEU performs spatial weight calibration on feature maps with richer spatial details to obtain spatially enhanced feature maps $F_{\text{seu}}^{bd}$. The PEU guides denoised feature maps to perform polarization weight calibration, resulting in polarization-enhanced feature maps $F_{\text{peu}}^{ad}$. Subsequently, the above two enhanced feature maps are input into the IFSU. This unit generates spatial weights using the feature maps enhanced by spatial information before despeckling and then injects spatial information flow into the feature maps after despeckling to guide its spatial information reconstruction. In parallel, it generates polarization weights using the despeckled feature map enhanced by polarization information, exchanging polarization information flow to promote the polarization features optimization and speckle noise weakening of the feature maps before despeckling. By switching the information flow of the dominant features between the two, the efficient fusion of the dominant characteristics before and after despeckling is achieved.

IFSU can improve the spatial texture information while maintaining the consistency of the polarization information of the feature maps, which can be mathematically expressed as

$$F_{\text{ifsu}} = f_{\text{cat}}\begin{pmatrix} f_{\text{mul}}\left(F_{\text{peu}}^{ad}, \xi\left(F_{\text{seu}}^{bd} \circ w_{\text{ifsu}}^{1} + b_{\text{ifsu}}^{1}\right)\right) \\ f_{\text{mul}}\left(F_{\text{seu}}^{bd}, \xi\left(F_{\text{peu}}^{ad} \circ w_{\text{ifsu}}^{2} + b_{\text{ifsu}}^{2}\right)\right) \end{pmatrix} \tag{12}$$

where $F_{\text{seu}}^{bd}$ is the spatial-enhanced feature maps before despeckling and $F_{\text{peu}}^{ad}$ is the polarization-enhanced feature map after despeckling. $w_{\text{ifsu}}^{1}$ and $b_{\text{ifsu}}^{1}$ represent the weight and bias terms of the $1 \times 1$ convolution layer. $w_{\text{ifsu}}^{2}$ and $b_{\text{ifsu}}^{2}$ are the weight and bias terms of the fully connected layer.

### E. Adaptive Joint Loss Function Based on Temporal Changes

Through the dual-polarization SAR despeckling framework under real data conditions, the nonlinear mapping relationship from dual-polarization SAR noisy images to dual-polarization SAR noise-free images can be established, represented mathematically as

$$\hat{C}_x = \xi\left(C_y\right) \tag{13}$$

where $C_y$ represents the noise covariance matrix, $\xi(.)$ indicates the proposed network model, and $\hat{C}_x$ denotes the denoising covariance matrix. Considering the large dynamic range of the SAR covariance matrix and the spatiotemporal differences of real training data, the Charbonnier loss function is adopted as the basis to construct the adaptive joint loss function based on temporal changes, which is specifically expressed as

$$L_t(\Theta) = \alpha L_n(\Theta) + \beta L_e(\Theta) \tag{14}$$

where $L_t(\Theta)$ is the proposed adaptive joint loss function, and $L_n(\Theta)$ denotes the numerical loss function, which is used to constrain the numerical consistency of the denoising results and the multitemporal mean label data. $L_e(\Theta)$ represents the edge information loss function, which is used to maintain the edge detail information of the denoising result. $\alpha$ and $\beta$ are nonnegative adaptive regularization parameters, determined as follows, and are used to adaptively optimize the weight:

$$\alpha = \frac{L_n(\Theta)}{L_n(\Theta) + L_e(\Theta)}, \quad \beta = \frac{L_e(\Theta)}{L_n(\Theta) + L_e(\Theta)}. \tag{15}$$

The numerical loss function can be depicted as

$$L_n(\Theta) = \frac{1}{N}\sum_{i=1}^{N} m_{tc}^i \cdot \sqrt{\left\| C_x^i - \xi\left(C_y^i\right)\right\|^2 + \varepsilon^2} \tag{16}$$

where $N$ is the number of training data pairs $\{C_y^i, C_x^i\}$, $C_y^i$ represents the $i$th covariance matrix with speckle noise, and $C_x^i$ represents the $i$th noise-free covariance matrix. $m_{tc}^i$ denotes the change detection mask, which is generated by the derivation of statistical similarity parameters on multitemporal SAR data. In this article, PolSAR pro v5.0 software is used to obtain change detection masks $m_{tc}^i$. $\varepsilon$ is a constant term, which is set to $10^{-3}$ in the proposed network.

The edge information loss function can be expressed as

$$L_e(\Theta) = \frac{1}{N}\sum_{i=1}^{N} m_{tc}^i \cdot \sqrt{\left\| \Delta\left(C_x^i\right) - \Delta\left(\xi\left(C_y^i\right)\right)\right\|^2 + \varepsilon^2} \tag{17}$$

where $\Delta(.)$ represents the Laplacian edge information extraction operator.

## IV. Comparison and Evaluation Experiments

In order to comprehensively demonstrate the effectiveness of the IFSDN model under diverse land surface conditions, we conducted spatial information retention experiments and polarization information analysis experiments on dual-polarization SAR images acquired by Sentinel-1 in different seasons. Besides, model generalization experiments are conducted in various cities across different climate zones.

### A. Experimental Data and Parameter Settings

In this article, the sample dataset generated in Section III-A is used for both training and testing. As shown in Table II, data from the four seasons of July 1, 2020; October 5, 2020; January 9, 2021; and April 3, 2021 are selected as noise data. The data of the ten adjacent time phases (the five phases before and after the target date) are statistically averaged to generate label data. A change detection mask is also generated based on the target time. Subsequently, the "noisy data-label data-change detection mask" is paired to generate a training dataset. The size of each data used in training is 8500 × 9200 × 4. For the convenience of training, it is cropped into 40 × 40 × 4 patches. There are a total of 194 944 patches for the four seasons. Similarly, data from July 13, 2020; October 17, 2020; January 21, 2021; and April 15, 2021, are selected to generate the test dataset. The size of each Sentinel-1 test data is 8000 × 8000 × 4, covering four seasons. In order to ensure the fairness of the experiment, there is no overlap between the training data and the test data. In addition, dual-polarization SAR images from Xi'an, Guangzhou and Hainan Island are selected as generalization experimental data. The size of these data is also 8000 × 8000 × 4. To verify the sensor generalization, L-band ALOS2 and X-band TerraSAR-X data are used to verify the despeckling performance of the proposed model. The size of ALOS2 data is 2000 × 2000 × 4, and the size of TerraSAR-X data is 1000 × 1000 × 4.

The IFSDN is trained in the Windows environment, using Pytorch1.10.0 and NVIDIA GeForce RTX 3080 GPU with a maximum memory of 64 GB. During the training, kaiming normal [46] is adopted for convolution kernel initialization, and Adam [47] is employed for network optimization. The training runs for 200 epochs, with an initial learning rate set to $10^{-3}$, which decreases by one-tenth every five epochs.

### B. Comparison Algorithms and Quantitative Indicators

In the spatial information preservation experiment, five mainstream despeckling methods are adopted for comparison with the proposed IFSDN, including PPB [48], MuLoG-BM3D [38], MuLoG-TV [38], SARDRN [34], deSpeckNet [33]. The PPB and MuLoG-BM3D are nonlocal mean filtering algorithms. MuLoG-TV is a total variation-based despeckling method under the MuLoG framework. SARDRN and deSpeckNet are learning-based despeckling methods. In terms of quantitative indicators, five commonly used metrics, namely, mean absolute error (MAE), mean relative error (MRE), log Euclidean metric (LEM), edge preservation degree on the ratio of average (EPD-ROA), and the equivalent number of looks (ENLs) are employed for evaluating despeckling capability. For the aforementioned indicators, MAE, MRE, and LEM are reference-based quantitative indicators, while EPD-ROA and ENL are reference-free quantitative indicators. Lower values of MAE and MRE signify a smaller error between the denoised result and the reference image. LEM is a commonly used measure in Riemannian manifolds and measures the distance between two covariance matrices. A smaller LEM value indicates that the two covariance matrices are closer. A higher EPD-ROA reflects greater spatial detail fidelity, while a higher ENL indicates better smoothing of homogeneous areas. The MAE can be formulated as

$$\mathrm{MAE} = \frac{1}{M}\sum_{i=1}^{M}\left|C_{\mathrm{mt}}^i - C_d^i\right| \tag{18}$$

where $C_d$ and $C_{\mathrm{mt}}$ respectively represent the despeckled results and the multitemporal composite reference image, and $M$ is the number of pixels.

The MRE can be mathematically expressed as

$$\mathrm{MRE} = \frac{1}{M}\sum_{i=1}^{M}\left|\frac{C_{\mathrm{mt}}^i - C_d^i}{C_{\mathrm{mt}}^i}\right|. \tag{19}$$

The LEM can be calculated by the following formula:

$$\mathrm{LEM} = \frac{1}{M}\sum_{i=1}^{M}\left\|\log\left(C_{\mathrm{mt}}^i\right) - \log\left(C_d^i\right)\right\|_F^2. \tag{20}$$

The EPD-ROA is depicted as

$$\mathrm{EPD\text{-}ROA} = \frac{\sum_{i=1}^{M}\left|I_{d,j,h}^i / I_{d,j,v}^i\right|}{\sum_{i=1}^{M}\left|I_{y,j,h}^i / I_{y,j,v}^i\right|}, \quad j = \mathrm{VV\ or\ VH} \tag{21}$$

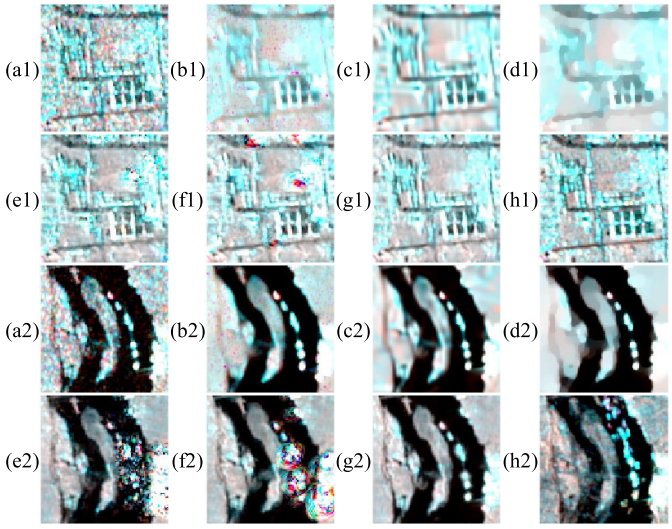


Fig. 5. Despeckling results in urban areas. (a) Original image with speckle. (b)–(g) Despeckling results of the PPB, the MuLoG-BM3D, the MuLoG-TV, the SARDRN, the deSpeckNet, and the proposed IFSDN method, respectively. (h) Multitemporal average image. (a1)–(h1) and (a2)–(h2) Enlarged images of the corresponding area.

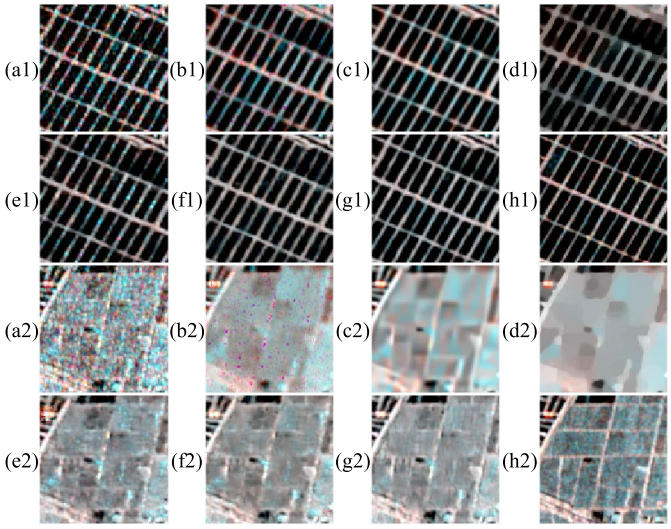


Fig. 6. Despeckling results in farmland areas. (a) Original image with speckle. (b)–(g) Despeckling results of the PPB, the MuLoG-BM3D, the MuLoG-TV, the SARDRN, the deSpeckNet, and the proposed IFSDN method, respectively. (h) Multitemporal average image. (a1)–(h1) and (a2)–(h2) Enlarged images of the corresponding area.

where the subscript $j$ indicates polarization mode, it represents VV and VH polarization, respectively. $I^i_{d,j,h}$ and $I^i_{y,j,h}$ represent the adjacent pixel values in the horizontal direction of despeckled and noisy SAR intensity image, respectively. $I^i_{d,j,v}$ and $I^i_{y,j,v}$, respectively, denote the adjacent pixel values in the vertical direction of despeckled and noisy SAR intensity image.

The ENL can be defined as

$$\mathrm{ENL} = \frac{\mu^2}{\sigma^2} \tag{22}$$

where $\mu$ and $\sigma$ represent the mean and standard deviation of the target homogeneous area within the SAR intensity image.

### C. Spatial Information Retention Experiment

In order to verify the speckle suppression ability and spatial information retention ability of the proposed method, a spatial information experiment is constructed. This experiment involved despeckling dual-polarization SAR images, followed by both visual and quantitative evaluations. The visual evaluation experiment includes a visual evaluation of RGB synthesis results of despeckling results and corresponding ENLs mapping, as well as the visual evaluation of intensity images and corresponding ratio diagrams. The quantitative evaluation experiment includes the calculation of reference-based quantitative indicators between the despeckling results and the multitemporal average covariance matrix, as well as calculations of reference-free quantitative indicators. For the visual evaluation, three typical areas are selected: urban complex land coverage area, farmland area, and mountain area. Figs. 5–7 shows the RGB composite images of the speckle removal results of various methods. The R, G, and B bands of false color correspond to $C_{22}$, $|C_{11} - 2C_{12\_\mathrm{real}} + C_{22}|$, and $C_{11}$, respectively.

In the three groups of experiments, traditional methods achieved a higher degree of speckle removal but exhibited varying degrees of oversmoothing, particularly the TV method.

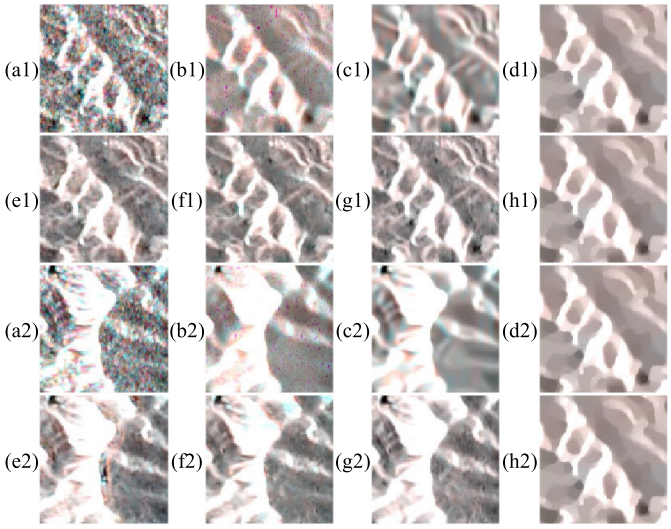


Fig. 7. Despeckling results in mountain areas. (a) Original image with speckle. (b)–(g) Despeckling results of the PPB, the MuLoG-BM3D, the MuLoG-TV, the SARDRN, the deSpeckNet, and the proposed IFSDN method, respectively. (h) Multitemporal average image. (a1)–(h1) and (a2)–(h2) Enlarged images of the corresponding area.

The PPB method, in contrast, introduced magenta spot-like artifacts after despeckling. Learning-based methods effectively preserved spatial information while removing speckle noise. SARDRN and deSpeckNet are, however, prone to color distortion when dealing with strong scattering point targets or areas with drastically varying backscattering coefficients. The proposed method outperformed others, closely approximating the multitemporal average image.

In urban built-up areas, as shown in Fig. 5(a1)–(h1), the PPB and MuLoG-BM3D methods show noticeable oversmoothing, and the MuLoG-TV suffered significant detail loss. SARDRN and deSpeckNet exhibited obvious artifacts in areas with strong scattering points. This issue was even more pronounced in Fig. 5(a2)–(h2), where SARDRN and deSpeckNet

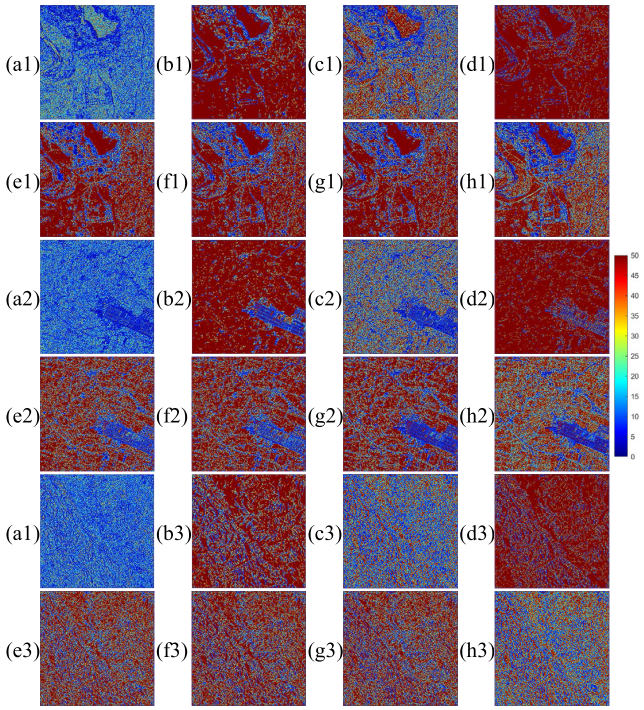


Fig. 8. ENL mapping. (a1)–(h1) ENL mapping of the original image with speckle, the PPB, the MuLoG-BM3D, the MuLoG-TV, the SARDRN, the deSpeckNet, the proposed IFSDN method, and the multitemporal average image in urban areas respectively. (a2)–(h2) and (a3)–(h3) ENL maps of the farmland area and the mountain area respectively.

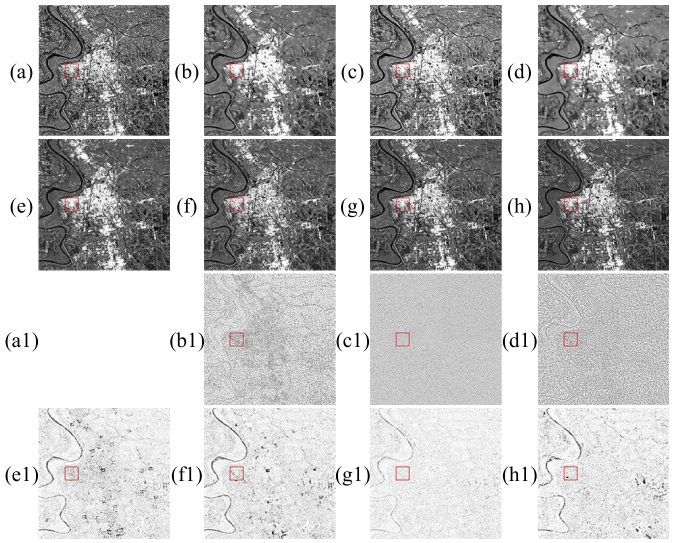


Fig. 9. Despeckled intensity image in complex land cover areas. (a) Original image with speckle. (b)–(g) Despeckling results of the PPB, the MuLoG-BM3D, the MuLoG-TV, the SARDRN, the deSpeckNet, and the proposed IFSDN method, respectively. (h) Multitemporal average image. (a1)–(h1) Corresponding ratio diagrams respectively.

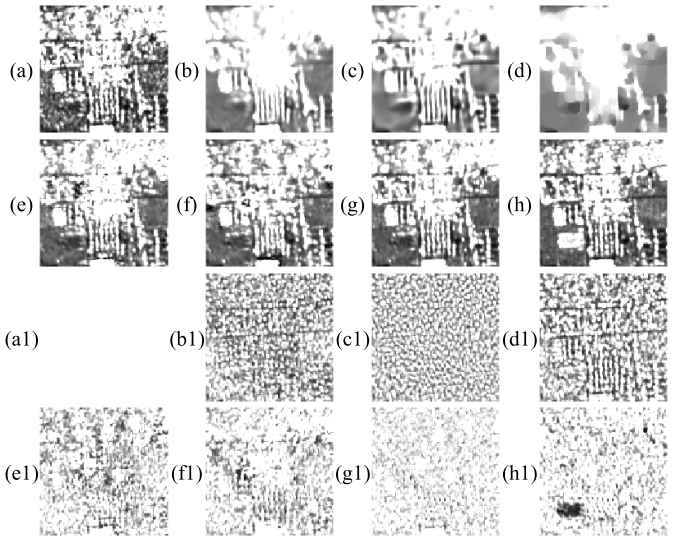


Fig. 10. Magnified image of despeckled intensity image in complex land cover areas. (a) Original image with speckle. (b)–(g) Despeckling results of the PPB, the MuLoG-BM3D, the MuLoG-TV, the SARDRN, the deSpeckNet, and the proposed IFSDN method, respectively. (h) Multitemporal average image. (a1)–(h1) Corresponding ratio diagrams respectively.

failed to denoise ships properly, leading to severe distortion of contour information. The proposed method excelled by effectively suppressing speckles while maintaining spatial detail and color information. The inadequacy of multitemporal averaged images in areas with drastically changing ground objects or moving targets further emphasized the necessity of a single-temporal speckle removal approach.

In the farmland area, depicted in Fig. 6(a1)–(h1), the PPB and MuLoG-BM3D methods produce nonuniform colors along field ridges, while MuLoG-TV shows defocusing, and SARDRN exhibits abnormally high values in some ridges. Both deSpeckNet and the proposed IFSDN effectively suppress noise in paddy fields, preserving the structured information of field ridges more completely. In Fig. 6(a2)–(h2), learning-based methods outperform traditional ones, balancing denoising with spatial detail preservation. In mountainous areas, as illustrated in Fig. 7, similar patterns are observed. The spot-like artifacts still exist in the PPB method, while the MuLoG-BM3D and MuLoG-TV methods suffer from serious texture information loss. Fig. 7(e3) indicates that SARDRN has outliers near the ridge line. The results of deSpeckNet and IFSDN have clear ridge lines and rich mountain texture details, aligning more closely with multitemporal average results.

ENL mapping results are shown in Fig. 8 to better demonstrate the despeckling performance of different methods in homogeneous areas and heterogeneous areas. All methods improve image visual quality to varying degrees. The PPB and MuLoG-TV methods achieve strong smoothing but lose significant spatial details in high-frequency areas like urban built-up zones. MuLoG-BM3D preserves spatial details better. Learning-based methods provide a better balance between speckle removal and detail preservation, with high ENL in smooth areas and lower ENL in heterogeneous regions such as built-up zones, field ridges, and ridgelines.

Intensity image and ratio diagrams experiments are constructed to observe spatial structure information leakage in areas with complex land cover. As shown in Figs. 9 and 10, PPB, MuLoG-BM3D, and MuLoG-TV exhibit significant structural information leakage. PPB's leakage is concentrated in urban and river-edge areas, while MuLoG-BM3D and MuLoG-TV show more uniform leakage across various land types. Learning-based methods experience some information loss near river contours. SARDRN and deSpeckNet introduce artifacts in urban areas, causing texture detail loss. In contrast,

TABLE III
QUANTITATIVE EVALUATION RESULTS OF VARIOUS DESPECKLING METHODS

| Method | PPB | MuLoG-BM3D | MuLoG-TV | SARDRN | deSpeckNet | IFSDN |
|---|---|---|---|---|---|---|
| MAE | **0.027** | 0.029 | 0.035 | 0.028 | 0.030 | **0.027** |
| MRE | 0.365 | 0.398 | 0.484 | 0.344 | 0.375 | **0.306** |
| LEM | 0.542 | 0.317 | 0.333 | 0.227 | 0.234 | **0.156** |
| EPD-ROA | 0.916 | 0.923 | 0.913 | 0.949 | **0.956** | 0.923 |
| ENL | 125.858 | 57.838 | **212.533** | 90.162 | 85.904 | 104.018 |

the proposed method's ratio diagrams are closer to 1, indicating better spatial structure preservation. It is worth noting that due to objects changing, the spatial information of the multitemporal average image in some areas differs from the noisy image.

In the quantitative evaluation experiment, as shown in Table III, the proposed method has smaller errors and achieved optimal results in the three quantitative indicators: MAE and MRE for intensity images and LEM for covariance matrix. In the speckle removal task, there is a trade-off between spatial information preservation and filtering smoothness. The SARDRN and deSpeckNet methods with higher EPD-ROA have relatively lower ENL, while the PPB and MuLoG-TV methods with higher ENL have relatively lower EPD-ROA. The proposed method can better balance spatial information preservation and speckle suppression and achieves the third-best performance in both EPD-ROA and ENL.

### D. Polarization Information Analysis Experiment

Polarization information reveals the geometric structure and physical properties of targets, making it crucial for assessing despeckling performance in polarimetric SAR images. By decomposing the polarization scattering matrix into fundamental components, polarization decomposition uncovers the intrinsic scattering mechanisms of targets. This study uses HAA polarization decomposition [49] methods to analyze and verify the IFSDN method's ability to preserve polarization information by analyzing the entropy (H), anisotropy (A), and mean alpha angle ($\alpha$). These parameters, sensitive to scattering mechanisms, help evaluate polarization retention before and after despeckling. Sentinel-1 dual-polarization SAR images are classified using the H/Alpha/A Wishart method based on the system in [50]. Fig. 11 shows three object classes: yellow (low-entropy multiple scattering, urban areas), blue (low-entropy surface scattering, water bodies), and green (low-entropy volume scattering, vegetation).

In Fig. 11(a), noise causes fragmented object representation, whereas Fig. 11(b)–(h) shows more cohesive classifications for denoised images. The PPB and MuLoG-TV methods produce overly smooth results, losing urban area boundaries. MuLoG-BM3D and SARDRN expand water areas, indicating altered backscattering coefficients, while deSpeckNet struggles with slender water bodies. IFSDN closely matches multitemporal average images, preserving object morphologies effectively. In Fig. 12, IFSDN and MuLoG-TV results show compact scatter plots on the H-Alpha plane, indicating better clustering for different object types. Other methods display more dispersed plots, highlighting IFSDN's superior discrimination capabilities for accurate image interpretation.

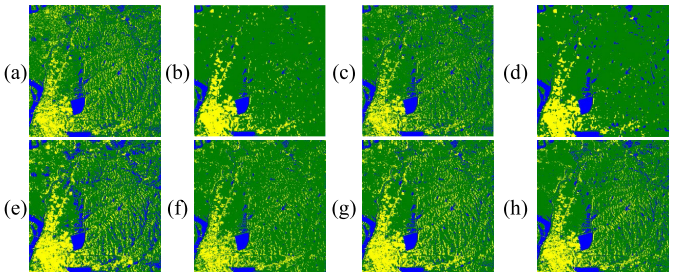


Fig. 11. HAA Wishart classification results. (a)–(h) Original image with speckle, the PPB, the MuLoG-BM3D, the MuLoG-TV, the SARDRN, the deSpeckNet, the IFSDN method, and the multitemporal average image. Among them, the yellow area represents the urban area, the blue area represents the water area, and the green area represents vegetation.

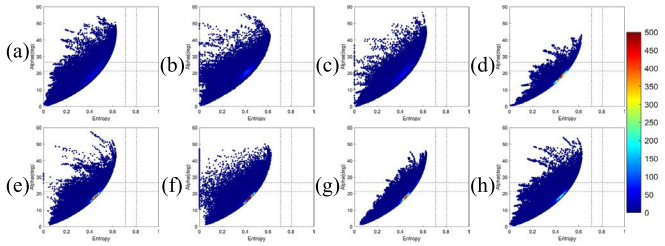


Fig. 12. H-alpha plane. (a)–(h) Original image with speckle, the PPB, the MuLoG-BM3D, the MuLoG-TV, the SARDRN, the deSpeckNet, the IFSDN method, and the multitemporal average image.

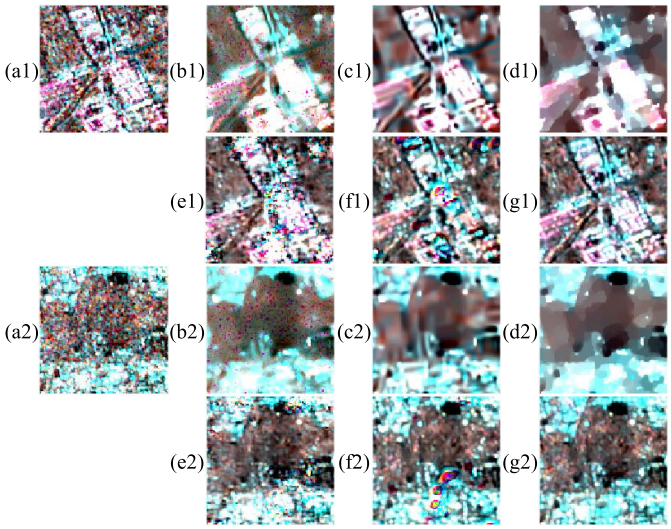


Fig. 13. Despeckling results in Xi'an area. (a1) and (a2) Original images with speckle. (b1)–(g1) and (b2)–(g2) Despeckling results of the PPB, the MuLoG-BM3D, the MuLoG-TV, the SARDRN, the deSpeckNet, and the IFSDN method in different areas.

### E. Generalization Evaluation Experiments

In order to verify the generalization performance of the proposed model, data from different climate zones are used to evaluate its robustness. Dual-polarization SAR images from three typical regions, namely, Xi'an in the temperate monsoon region, Guangzhou in the subtropical monsoon region, and Hainan Island in the tropical monsoon region, are selected for generalization evaluation experiments.

As shown in Figs. 13–15, the PPB method results across all three regions exhibit varying degrees of magenta noise. The MuLoG-BM3D method and MuLoG-TV can effectively

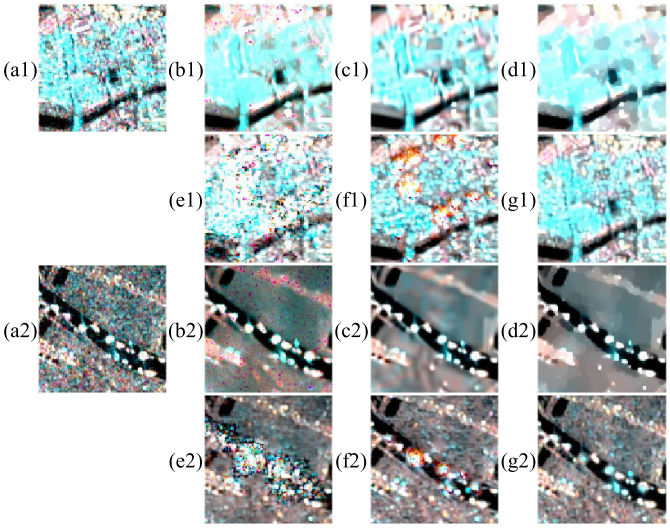


Fig. 14. Despeckling results in Guangzhou area. (a1) and (a2) Original images with speckle. (b1)–(g1) and (b2)–(g2) Despeckling results of the PPB, the MuLoG-BM3D, the MuLoG-TV, the SARDRN, the deSpeckNet, and the IFSDN method in different areas.

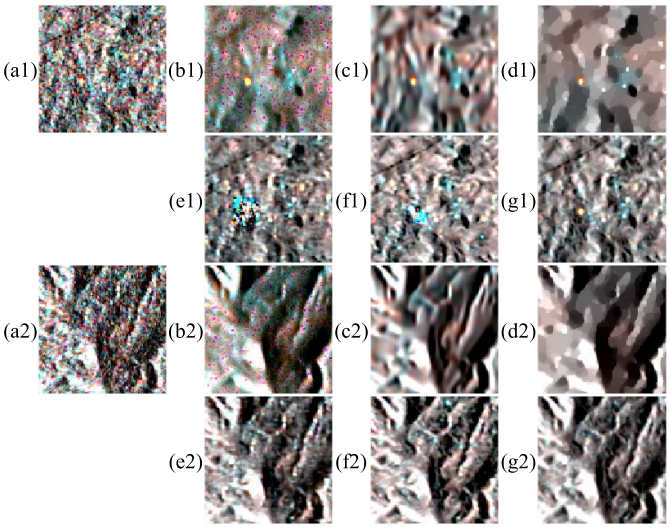


Fig. 15. Despeckling results in Hainan Island. (a1) and (a2) Original images with speckle. (b1)–(g1) and (b2)–(g2) Despeckling results of the PPB, the MuLoG-BM3D, the MuLoG-TV, the SARDRN, the deSpeckNet, and the IFSDN method in different areas.

remove speckle noise but cause obvious structural information loss and oversmoothing. The SARDRN and deSpeckNet have obvious artifacts in urban built-up areas, particularly in Xi'an and Guangzhou. In addition, both SARDRN and deSpeckNet poorly preserve strong scattering points and exhibit prominent artifacts in high backscattering coefficient areas, as shown in the enlarged images of Figs. 13 and 14. Conversely, the proposed method performs well across all three climate zones, effectively removing speckle noise while retaining spatial detail information with minimal reconstruction error. Table IV presents the quantitative evaluation results for each region, using reference-free indicators for evaluation. The quantitative results demonstrate that in all three regions, the proposed method can effectively balance the despeckling performance and the spatial detail preservation, indicating its superior robustness over the comparison methods.

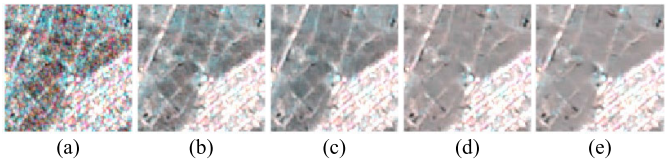


Fig. 16. Despeckling results under different phase numbers. (a)–(e) Noisy images, the despeckling results of 7t, 11t, 21t, and 31t data, respectively.

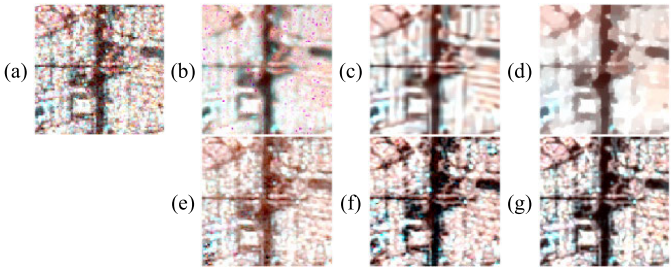


Fig. 17. Despeckling results of ALOS2 data. (a) Original image with speckle. (b)–(g) Despeckling results of the PPB, the MuLoG-BM3D, the MuLoG-TV, the SARDRN, the deSpeckNet, and the IFSDN method, respectively.

## V. Discussion

### A. Phase Quantity Sensitivity Analysis

In order to investigate the impact of the phase numbers on the labeled data generation, this study analyzes the performance of labeled datasets constructed with varying phase counts, using Sentinel-1 data from July 1, 2020, as the target date data. Datasets are constructed with 7, 11, 21, and 31 phases, corresponding to three, five, ten, and 15 phases before and after the target date, respectively, labeled as 7t, 11t, 21t, and 31t. The IFSDN network is retrained with these datasets and tested on Sentinel-1 data from July 13, 2020.

As shown in Table V, increasing the number of phases improves noise suppression and significantly enhances the ENL; however, this comes at the cost of losing edge details, leading to a decrease in EPD-ROA. Visual results in Fig. 16 show that as the number of phases increases, the despeckling results become smoother, and noise reduction improves. A larger number of phases and a longer time span, however, introduce seasonal changes, causing variations in the backscattering coefficient and resulting in color distortion in the despeckling results. In Fig. 16, compared to the original noisy image, the 7t and 11t datasets, averaged within the same season, show minimal color distortion and maintain intensity in farmland areas closer to the original. In contrast, the 21t and 31t datasets, derived from cross-seasonal data, exhibit brightening in farmland areas, indicating stronger backscattering coefficients. In order to balance noise suppression and minimize color distortion, this study uses the 11-phase average dataset, covering approximately one season, as the label data to mitigate the effects of seasonal changes.

### B. Generalization Experiments Across Sensors

In order to verify the cross-sensor despeckle performance of IFSDN, the L-band ALOS-2 and X-band TerraSAR data are adopted to construct a generalization experiment. Fig. 17 shows despeckling results for ALOS-2 urban areas. Traditional methods can effectively reduce noise, but they

TABLE IV
QUANTITATIVE EVALUATION RESULTS OF VARIOUS DESPECKLING METHODS ACROSS VARIOUS CLIMATE ZONES

| | Method | PPB | MuLoG-BM3D | MuLoG-TV | SARDRN | deSpeckNet | IFSDN |
|---|---|---|---|---|---|---|---|
| XA | EPD-ROA | 0.814 | 0.815 | 0.806 | **1.001** | 0.919 | 0.829 |
| | ENL | 46.344 | 28.202 | **58.133** | 15.362 | 3.620 | 17.491 |
| GZ | EPD-ROA | 0.751 | 0.753 | 0.736 | 1.208 | **0.811** | 0.773 |
| | ENL | 64.931 | 43.982 | **85.366** | 11.630 | 8.255 | 13.089 |
| HN | EPD-ROA | 0.817 | 0.821 | 0.813 | **0.858** | 0.835 | 0.829 |
| | ENL | 54.865 | 28.636 | **132.325** | 15.950 | 15.504 | 16.839 |

Note: XA stands for Xi'an, GZ stands for Guangzhou, and HN stands for Hainan Island.

TABLE V
QUANTITATIVE EVALUATION RESULTS OF PHASE QUANTITY SENSITIVITY ANALYSIS

| Method | ENL | EPD-ROA |
|---|---|---|
| IFSDN-7t | 61.006 | 0.934 |
| IFSDN-11t | 108.601 | 0.927 |
| IFSDN-21t | 120.373 | 0.925 |
| IFSDN-31t | 157.130 | 0.923 |

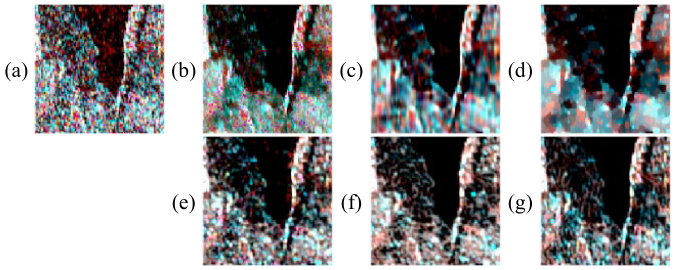


Fig. 18. Despeckling results of TerraSAR data. (a) Original image with speckle. (b)–(g) Despeckling results of the PPB, the MuLoG-BM3D, the MuLoG-TV, the SARDRN, the deSpeckNet, and the IFSDN method, respectively.

TABLE VI
QUANTITATIVE EVALUATION RESULTS OF GENERALIZATION EXPERIMENTS ACROSS SENSORS

| | Method | PPB | MuLoG-BM3D | MuLoG-TV | SARDRN | deSpeckNet | IFSDN |
|---|---|---|---|---|---|---|---|
| ALOS2 | EPD-ROA | 0.707 | 0.707 | 0.694 | **0.921** | 0.792 | 0.742 |
| | ENL | 47.807 | 22.471 | **80.271** | 5.347 | 45.282 | 45.635 |
| TerraSAR | EPD-ROA | 0.485 | 0.483 | 0.464 | **0.518** | 0.509 | 0.506 |
| | ENL | 12.506 | 9.913 | 16.868 | 6.064 | 12.630 | **23.703** |

struggle to retain structural details, blurring building outlines. Deep learning methods preserve texture better, but SARDRN introduces color distortion, and deSpeckNet fails to fully suppress road noise. The proposed method successfully balances noise suppression with texture preservation. Fig. 18 presents TerraSAR despeckling results, where speckle noise is more intense. In water areas, all methods except SARDRN remove speckles effectively. PPB, however, produces magenta artifacts, and MuLoG-BM3D and MuLoG-TV over-smooth the results. Both deSpeckNet and IFSDN achieve a good balance between noise removal and detail retention. As shown in Table VI, performance on ALOS-2 data is relatively better, but in TerraSAR data, the higher noise intensity reduces overall despeckling effectiveness and spatial detail retention. The proposed method maintains a balance between noise suppression and detail preservation for both datasets.

## VI. CONCLUSION

This article proposes an IFSDN framework tailored for real SAR image conditions. Under this framework, the long-time series SAR images from Sentinel-1 are temporally synthesized to generate the "noisy-temporal average label" dual-polarization SAR dataset for sample data. The HFEM is constructed to independently process and integrate features from each element of the covariance matrix, thereby preventing information interference between polarization channels. The multihierarchical residual attention module is designed to effectively extract and recalibrate feature maps from low to high levels. An innovative information flow switching mechanism is constructed to exchange beneficial information dominated by features before and after denoising. This mechanism guides the spatial information reconstruction of despeckled feature maps, weakens the noise impact on predenoised feature maps, and maintains polarization information. Additionally, an adaptive joint loss function, which considers the changing relationship of ground objects in multitemporal data, is constructed to eliminate the difference in backscattering coefficients caused by changes in ground objects and constrain the network training process. The spatial information retention experiments and polarization information analysis experiments indicate that the IFSDN model is superior to the existing state-of-the-art methods in both visual comparison and quantitative evaluation. The proposed method has excellent spatial-polarization information retention capabilities, lower errors in speckle suppression, and fewer artifacts.

Because of data availability constraints, the proposed method primarily targets Sentinel-1 dual-polarization SAR images. The focus of subsequent research is to improve the applicability of the proposed method and extend it to full-polarimetric SAR image despeckling tasks. In addition, future work will also focus on the coupling task of the scattering mechanism and learning mechanism.

## ACKNOWLEDGMENT

The authors would like to thanks European Space Agency (ESA) for providing Sentinel-1 Dual-polarization Synthetic Aperture radar (SAR) data. They would also like to thank Zihan Qin from Wuhan University for her valuable assistance with this article.

## REFERENCES

[1] J.-S. Lee and E. Pottier, *Polarimetric Radar Imaging: From Basics To Applications*. Boca Raton, FL, USA: CRC Press, 2017.

[2] L. Lin, H. Shen, J. Li, and Q. Yuan, "FDFNet: A fusion network for generating high-resolution fully PolSAR images," *IEEE Geosci. Remote Sens. Lett.*, vol. 19, pp. 1–5, 2022, doi: 10.1109/LGRS.2021.3127958.

[3] K. Jin, Y. Chen, B. Xu, J. Yin, X. Wang, and J. Yang, "A patch-to-pixel convolutional neural network for small ship detection with PolSAR images," *IEEE Trans. Geosci. Remote Sens.*, vol. 58, no. 9, pp. 6623–6638, Sep. 2020, doi: 10.1109/TGRS.2020.2978268.

[4] C. Liu and C. H. Gierull, "A new application for PolSAR imagery in the field of moving target indication/ship detection," *IEEE Trans. Geosci. Remote Sens.*, vol. 45, no. 11, pp. 3426–3436, Nov. 2007, doi: 10.1109/TGRS.2007.907192.

[5] S. Plank, "Rapid damage assessment by means of multi-temporal SAR—A comprehensive review and outlook to Sentinel-1," *Remote Sens.*, vol. 6, no. 6, pp. 4870–4906, May 2014, doi: 10.3390/rs6064870.

[6] L. Zhao, J. Yang, P. Li, L. Zhang, L. Shi, and F. Lang, "Damage assessment in urban areas using post-earthquake airborne PolSAR imagery," *Int. J. Remote Sens.*, vol. 34, no. 24, pp. 8952–8966, Dec. 2013, doi: 10.1080/01431161.2013.860566.

[7] X. Liu, L. Jiao, X. Tang, Q. Sun, and D. Zhang, "Polarimetric convolutional network for PolSAR image classification," *IEEE Trans. Geosci. Remote Sens.*, vol. 57, no. 5, pp. 3040–3054, May 2019, doi: 10.1109/TGRS.2018.2879984.

[8] Z. Qi, A. G.-O. Yeh, X. Li, and Z. Lin, "A novel algorithm for land use and land cover classification using RADARSAT-2 polarimetric SAR data," *Remote Sens. Environ.*, vol. 118, pp. 21–39, Mar. 2012, doi: 10.1016/j.rse.2011.11.001.

[9] G. Liu, B. Liu, G. Zheng, and X. Li, "Environment monitoring of Shanghai nanhui intertidal zone with dual-polarimetric SAR data based on deep learning," *IEEE Trans. Geosci. Remote Sens.*, vol. 60, 2022, Art. no. 4208918, doi: 10.1109/TGRS.2022.3197149.

[10] X. Ma, J. Xu, P. Wu, and P. Kong, "Oil spill detection based on deep convolutional neural networks using polarimetric scattering information from Sentinel-1 SAR images," *IEEE Trans. Geosci. Remote Sens.*, vol. 60, 2022, Art. no. 4204713, doi: 10.1109/TGRS.2021.3126175.

[11] X. Ma, J. Xu, J. Pan, J. Yang, P. Wu, and X. Meng, "Detection of marine oil spills from radar satellite images for the coastal ecological risk assessment," *J. Environ. Manage.*, vol. 325, Jan. 2023, Art. no. 116637, doi: 10.1016/j.jenvman.2022.116637.

[12] H. Shen, C. Zhou, J. Li, and Q. Yuan, "SAR image despeckling employing a recursive deep CNN prior," *IEEE Trans. Geosci. Remote Sens.*, vol. 59, no. 1, pp. 273–286, Jan. 2021, doi: 10.1109/TGRS.2020.2993319.

[13] V. S. Frost, J. A. Stiles, K. S. Shanmugan, and J. C. Holtzman, "A model for radar images and its application to adaptive digital filtering of multiplicative noise," *IEEE Trans. Pattern Anal. Mach. Intell.*, vol. PAMI-4, no. 2, pp. 157–166, Mar. 1982, doi: 10.1109/TPAMI.1982.4767223.

[14] D. T. Kuan, A. A. Sawchuk, T. C. Strand, and P. Chavel, "Adaptive noise smoothing filter for images with signal-dependent noise," *IEEE Trans. Pattern Anal. Mach. Intell.*, vol. PAMI-7, no. 2, pp. 165–177, Feb. 1985, doi: 10.1109/TPAMI.1985.4767641.

[15] J.-S. Lee, "A simple speckle smoothing algorithm for synthetic aperture radar images," *IEEE Trans. Syst., Man, Cybern.*, vol. SMC-13, no. 1, pp. 85–89, Jan. 1983, doi: 10.1109/TSMC.1983.6313036.

[16] G. Vasile, E. Trouve, J.-S. Lee, and V. Buzuloiu, "Intensity-driven adaptive-neighborhood technique for polarimetric and interferometric SAR parameters estimation," *IEEE Trans. Geosci. Remote Sens.*, vol. 44, no. 6, pp. 1609–1621, Jun. 2006, doi: 10.1109/TGRS.2005.864142.

[17] J.-S. Lee, M. R. Grunes, and G. de Grandi, "Polarimetric SAR speckle filtering and its implication for classification," *IEEE Trans. Geosci. Remote Sens.*, vol. 37, no. 5, pp. 2363–2373, Sep. 1999, doi: 10.1109/36.789635.

[18] J.-S. Lee, T. L. Ainsworth, Y. Wang, and K.-S. Chen, "Polarimetric SAR speckle filtering and the extended sigma filter," *IEEE Trans. Geosci. Remote Sens.*, vol. 53, no. 3, pp. 1150–1160, Mar. 2015, doi: 10.1109/TGRS.2014.2335114.

[19] C.-A. Deledalle, L. Denis, and F. Tupin, "Iterative weighted maximum likelihood denoising with probabilistic patch-based weights," *IEEE Trans. Image Process.*, vol. 18, no. 12, pp. 2661–2672, Dec. 2009, doi: 10.1109/TIP.2009.2029593.

[20] S. Parrilli, M. Poderico, C. V. Angelino, and L. Verdoliva, "A nonlocal SAR image denoising algorithm based on LLMMSE wavelet shrinkage," *IEEE Trans. Geosci. Remote Sens.*, vol. 50, no. 2, pp. 606–616, Feb. 2012, doi: 10.1109/TGRS.2011.2161586.

[21] H. Zhong, J. Zhang, and G. Liu, "Robust polarimetric SAR despeckling based on nonlocal means and distributed lee filter," *IEEE Trans. Geosci. Remote Sens.*, vol. 52, no. 7, pp. 4198–4210, Jul. 2014, doi: 10.1109/TGRS.2013.2280278.

[22] L. I. Rudin, S. Osher, and E. Fatemi, "Nonlinear total variation based noise removal algorithms," *Phys. D, Nonlinear Phenomena*, vol. 60, nos. 1–4, pp. 259–268, 1992, doi: 10.1016/0167-2789(92)90242-F.

[23] O. Scherzer, M. Grasmair, H. Grossauer, M. Haltmeier, and F. Lenzen, *Variational Methods in Imaging*, vol. 167. Cham, Switzerland: Springer, 2009.

[24] G. Aubert and J.-F. Aujol, "A variational approach to removing multiplicative noise," *SIAM J. Appl. Math.*, vol. 68, no. 4, pp. 925–946, Jan. 2008.

[25] J. Shi and S. Osher, "A nonlinear inverse scale space method for a convex multiplicative noise model," *SIAM J. Imag. Sci.*, vol. 1, no. 3, pp. 294–321, Jan. 2008.

[26] X. Ma, H. Shen, X. Zhao, and L. Zhang, "SAR image despeckling by the use of variational methods with adaptive nonlocal functionals," *IEEE Trans. Geosci. Remote Sens.*, vol. 54, no. 6, pp. 3421–3435, Jun. 2016, doi: 10.1109/TGRS.2016.2517627.

[27] X. Nie, H. Qiao, and B. Zhang, "A variational model for PolSAR data speckle reduction based on the Wishart distribution," *IEEE Trans. Image Process.*, vol. 24, no. 4, pp. 1209–1222, Apr. 2015, doi: 10.1109/TIP.2015.2396292.

[28] E. Dalsasso, L. Denis, and F. Tupin, "SAR2SAR: A semi-supervised despeckling algorithm for SAR images," *IEEE J. Sel. Topics Appl. Earth Observ. Remote Sens.*, vol. 14, pp. 4321–4329, 2021, doi: 10.1109/JSTARS.2021.3071864.

[29] J. Li, L. Lin, M. He, J. He, Q. Yuan, and H. Shen, "Sentinel-1 dual-polarization SAR images despeckling network based on unsupervised learning," *IEEE Trans. Geosci. Remote Sens.*, vol. 62, 2024, Art. no. 5106315, doi: 10.1109/TGRS.2024.3404405.

[30] X. Ma, C. Wang, Z. Yin, and P. Wu, "SAR image despeckling by noisy reference-based deep learning method," *IEEE Trans. Geosci. Remote Sens.*, vol. 58, no. 12, pp. 8807–8818, Dec. 2020, doi: 10.1109/TGRS.2020.2990978.

[31] H. Shen, L. Lin, J. Li, Q. Yuan, and L. Zhao, "A residual convolutional neural network for polarimetric SAR image super-resolution," *ISPRS J. Photogramm. Remote Sens.*, vol. 161, pp. 90–108, Mar. 2020, doi: 10.1016/j.isprsjprs.2020.01.006.

[32] P. Wang, H. Zhang, and V. M. Patel, "SAR image despeckling using a convolutional neural network," *IEEE Signal Process. Lett.*, vol. 24, no. 12, pp. 1763–1767, Dec. 2017, doi: 10.1109/LSP.2017.2758203.

[33] A. G. Mullissa, D. Marcos, D. Tuia, M. Herold, and J. Reiche, "DeSpeckNet: Generalizing deep learning-based SAR image despeckling," *IEEE Trans. Geosci. Remote Sens.*, vol. 60, 2022, Art. no. 5200315, doi: 10.1109/TGRS.2020.3042694.

[34] Q. Zhang, Q. Yuan, J. Li, Z. Yang, and X. Ma, "Learning a dilated residual network for SAR image despeckling," *Remote Sens.*, vol. 10, no. 2, p. 196, Jan. 2018, doi: 10.3390/rs10020196.

[35] J. Li, Y. Li, Y. Xiao, and Y. Bai, "HDRANet: Hybrid dilated residual attention network for SAR image despeckling," *Remote Sens.*, vol. 11, no. 24, p. 2921, Dec. 2019, doi: 10.3390/rs11242921.

[36] G. Chierchia, D. Cozzolino, G. Poggi, and L. Verdoliva, "SAR image despeckling through convolutional neural networks," in *Proc. IEEE Int. Geosci. Remote Sens. Symp. (IGARSS)*, Jul. 2017, pp. 5438–5441, doi: 10.1109/IGARSS.2017.8128234.

[37] E. Dalsasso, X. Yang, L. Denis, F. Tupin, and W. Yang, "SAR image despeckling by deep neural networks: From a pre-trained model to an end-to-end training strategy," *Remote Sens.*, vol. 12, no. 16, p. 2636, Aug. 2020, doi: 10.3390/rs12162636.

[38] C.-A. Deledalle, L. Denis, S. Tabti, and F. Tupin, "MuLoG, or how to apply Gaussian denoisers to multi-channel SAR speckle reduction?" *IEEE Trans. Image Process.*, vol. 26, no. 9, pp. 4389–4403, Sep. 2017, doi: 10.1109/TIP.2017.2713946.

[39] D. Tucker and L. C. Potter, "Polarimetric SAR despeckling with convolutional neural networks," *IEEE Trans. Geosci. Remote Sens.*, vol. 60, 2022, Art. no. 5110712, doi: 10.1109/TGRS.2022.3152068.

[40] C. Lopez-Martinez and X. Fabregas, "Polarimetric SAR speckle noise model," *IEEE Trans. Geosci. Remote Sens.*, vol. 41, no. 10, pp. 2232–2242, Oct. 2003.

[41] A. A. Nielsen, M. J. Canty, H. Skriver, and K. Conradsen, "Change detection in multi-temporal dual polarization Sentinel-1 data," in *Proc. IEEE Int. Geosci. Remote Sens. Symp. (IGARSS)*, Fort Worth, TX, USA, Jul. 2017, pp. 3901–3908, doi: 10.1109/IGARSS.2017.8127854.

[42] J. Fu et al., "Dual attention network for scene segmentation," 2018, *arXiv:1809.02983*.

[43] L. Lin, Y. Shen, J. Wu, and F. Nan, "CAFE: A cross-attention based adaptive weighting fusion network for MODIS and Landsat spatiotemporal fusion," *IEEE Geosci. Remote Sens. Lett.*, vol. 20, pp. 1–5, 2023, doi: 10.1109/LGRS.2023.3286463.

[44] Y. Jing, L. Lin, X. Li, T. Li, and H. Shen, "An attention mechanism based convolutional network for satellite precipitation downscaling over China," *J. Hydrol.*, vol. 613, Oct. 2022, Art. no. 128388, doi: 10.1016/j.jhydrol.2022.128388.

[45] L. Lin, J. Li, H. Shen, L. Zhao, Q. Yuan, and X. Li, "Low-resolution fully polarimetric SAR and high-resolution single-polarization SAR image fusion network," *IEEE Trans. Geosci. Remote Sens.*, vol. 60, 2022, Art. no. 5216117, doi: 10.1109/TGRS.2021.3121166.

[46] K. He, X. Zhang, S. Ren, and J. Sun, "Delving deep into rectifiers: Surpassing human-level performance on ImageNet classification," in *Proc. IEEE Int. Conf. Comput. Vis. (ICCV)*, Santiago, Chile, Dec. 2015, pp. 1026–1034, doi: 10.1109/ICCV.2015.123.

[47] D. P. Kingma and J. Ba, "Adam: A method for stochastic optimization," 2014, *arXiv:1412.6980*.

[48] C.-A. Deledalle, L. Denis, F. Tupin, A. Reigber, and M. Jäger, "NL-SAR: A unified nonlocal framework for resolution-preserving (Pol)(In)SAR denoising," *IEEE Trans. Geosci. Remote Sens.*, vol. 53, no. 4, pp. 2021–2038, Apr. 2015, doi: 10.1109/TGRS.2014.2352555.

[49] S. R. Cloude and E. Pottier, "An entropy based classification scheme for land applications of polarimetric SAR," *IEEE Trans. Geosci. Remote Sens.*, vol. 35, no. 1, pp. 68–78, Feb. 1997, doi: 10.1109/36.551935.

[50] S. Salma, N. Keerthana, and B. M. Dodamani, "Target decomposition using dual-polarization Sentinel-1 SAR data: Study on crop growth analysis," *Remote Sens. Appl., Soc. Environ.*, vol. 28, Nov. 2022, Art. no. 100854, doi: 10.1016/j.rsase.2022.100854.

**Liupeng Lin** received the B.S. degree in geographical information science and the Ph.D. degree in cartography and geographic information engineering from Wuhan University, Wuhan, China, in 2017 and 2022, respectively.

He is currently a Hongyi Post-doctoral Researcher with the School of Resource and Environmental Sciences (SRES), Wuhan University. His research interests include SAR image reconstruction, remote sensing image processing and application, and data fusion.

**Huanfeng Shen** (Senior Member, IEEE) received the B.S. degree in surveying and mapping engineering and the Ph.D. degree in photogrammetry and remote sensing from Wuhan University, Wuhan, China, in 2002 and 2007, respectively.

He is currently a Hongyi Distinguished Professor with Wuhan University, where he is also the Dean of the School of Resource and Environmental Sciences. He was or is the PI of two projects supported by National Key Research and Development Program of China, and eight projects supported by the National Natural Science Foundation of China. He has authored or coauthored more than 200 journal citation report (JCR) papers and published five books as a Chief Editor. His papers received 16 269 citations in Web of Science (WoS) (as of May 2024). His research interests include remote sensing image processing, multisource data fusion, and intelligent environmental sensing.

Dr. Shen is a fellow of IET, the Deputy Director of the Remote Sensing Geography Committee of the Geographical Society of China, and the Deputy Director of the Big Data and Artificial Intelligence Committee of the Chinese Society for Geodesy, Photogrammetry, and Cartography. He is also a Senior Regional Editor of *Journal of Applied Remote Sensing* and an Editorial Board Members of *ISPRS Journal of Photogrammetry and Remote Sensing* and *Geo-Spatial Information Science*.

**Jie Li** (Member, IEEE) received the B.S. degree in sciences and techniques of remote sensing and the Ph.D. degree in photogrammetry and remote sensing from Wuhan University, Wuhan, China, in 2011 and 2016, respectively.

He is currently an Associate Professor with the School of Geodesy and Geomatics, Wuhan University. His research interests include image quality improvement, image superresolution reconstruction, data fusion, remote sensing image processing, sparse representation, and deep learning.

**Jingan Wu** received the B.S. degree in geographic information system from Anhui University, Hefei, China, in 2015, and the Ph.D. degree in cartography and geographic information engineering from Wuhan University, Wuhan, China, in 2021.

He is currently an Associate Research Fellow with the School of Geospatial Engineering and Science, Sun Yat-sen University, Zhuhai, China. His research interests include spatiotemporal data fusion and missing information reconstruction of remote sensing images.

**Shaowei Shi** received the B.S. degree in surveying and mapping engineering from the School of Geodesy and Geomatics, Wuhan University, Wuhan, China, in 2021, where he is currently pursuing the M.S. degree with the School of Geodesy and Geomatics.

His research interests include SAR image processing, denoising, change detection, and deep learning.

**Qiangqiang Yuan** (Member, IEEE) received the B.S. degree in surveying and mapping engineering and the Ph.D. degree in photogrammetry and remote sensing from Wuhan University, Wuhan, China, in 2006 and 2012, respectively.

In 2012, he joined the School of Geodesy and Geomatics, Wuhan University, where he is currently a Professor. He has published more than 90 research articles, including more than 70 peer reviewed articles in international journals, such as IEEE TRANSACTIONS ON IMAGE PROCESSING and IEEE TRANSACTIONS ON GEOSCIENCE AND REMOTE SENSING. His research interests include image reconstruction, remote sensing image processing and application, and data fusion.

Dr. Yuan was a recipient of the Top-Ten Academic Star of Wuhan University in 2011 and the Youth Talent Support Program of China in 2019. In 2014, he received the Hong Kong Scholar Award from the Society of Hong Kong Scholars and the China National Postdoctoral Council. He is on the Editorial Board of nine international journals and has frequently served as a referee for more than 50 international journals for remote sensing and image processing.